Journal of Sustainable Cement-Based Materials

ISSN: 2165-0373 (Print) 2165-0381 (Online) Journal homepage: www.tandfonline.com/journals/tscm20

Rheological, mechanical and fire resistance performance of waste glass activated geopolymers for concrete 3D printing

Sayanthan Ramakrishnan, Kirubajiny Pasupathy, Allan C. Manalo & Jay Sanjayan

To cite this article: Sayanthan Ramakrishnan, Kirubajiny Pasupathy, Allan C. Manalo & Jay Sanjayan (28 Jul 2025): Rheological, mechanical and fire resistance performance of waste glass activated geopolymers for concrete 3D printing, Journal of Sustainable Cement-Based Materials, DOI: 10.1080/21650373.2025.2529994

To link to this article: https://doi.org/10.1080/21650373.2025.2529994

Published online: 28 Jul 2025.

Journal of Sustainable Cement-Based Materials, 2025
http://dx.doi.org/10.1080/21650373.2025.2529994

Rheological, mechanical and fire resistance performance of waste glass activated geopolymers for concrete 3D printing

Sayanthan Ramakrishnan[a]*, Kirubajiny Pasupathy[b], Allan C. Manalo[a] and Jay Sanjayan[c]

[a]*Centre for Future Materials, School of Engineering, University of Southern Queensland, Toowoomba, Queensland, Australia;* [b]*SMEC Australia, Docklands, Victoria, Australia;* [c]*Centre for Sustainable Infrastructure and Digital Construction, School of Engineering, Swinburne University of Technology, Hawthorn, Victoria, Australia*

(Received 3 April 2025; Accepted 2 July 2025)

This study investigates the alkali activation of waste glass powder (WGP) for developing 3D printable geopolymer concrete. The rheological, mechanical, and fire-resistance of 3D printed concrete were evaluated to determine the effect of WGP as a partial substitution for fly ash in geopolymers. Rheological results show that incorporation of WGP reduces the rheological properties of printable mixes. For instance, the apparent viscosity of mixes containing 50% WGP was reduced by 48% at low shear rate ($0.1\,s^{-1}$), and 46% at high shear rate ($100\,s^{-1}$). The corresponding reductions in the dynamic yield stress and plastic viscosity were 35% and 55%, respectively, indicating improved flowability and pumpability. However, compressive strength declined with increased WGP. The 28-day mold-cast strength decreased from 51.4 MPa to 35.6 MPa at 50% WGP. In contrast, the elevated temperature properties are enhanced with reduced strength loss for the WGP incorporated specimens, attributed to the sintering effect of WGP. .

Keywords: waste glass powder; rheological properties; digital construction; porosity; sustainability

1. Introduction

Glass products are one of the most important commodities in the building and consumer products industry, and their production rate is continuously increasing due to increasing demand. As a result, the disposal of waste glass has become a major threat to the environment. Although waste glass can be recycled without losing its quality, large volumes of glass waste are still disposed of in landfills [1]. For instance, Australia generated 1.54 Mt of glass waste in the period of 2020–2021, with only 59% of glass waste recycled, while the remaining amount is being stockpiled and landfilled [2]. Globally, the European Union countries are leading in waste glass recycling with a recycling rate of 73%, however, other major consumers such as the US and Singapore are recycling at a low rate [3]. One of the major barriers to conventional glass recycling is the difficulty in separating various glass sources from the waste collection. The mixed glass sources contain different glass types, which will have different melting temperatures, viscosity after melting and other key properties required for molding and extrusion. This makes it extremely difficult to produce glass products of good quality. Therefore, alternative methods without remelting the glass are necessary to increase the recycling rates.

In recent years, the recycling of waste glass as a substitution to building material has received significant attention [1,4–6]. The glass waste has been converted into different forms, such as glass fibers [7–9], waste glass sand [10,11], etc. Similar to sand, glass also primarily consists of silica, which makes it an ideal substitution for sand (fine aggregate) in concrete. Past studies indicate that the substitution of conventional aggregate with waste glass could enhance the strength of concrete. This enhancement is attributed to the robustness and surface characteristics of glass aggregate, which offers a greater surface area with the cement paste. As a result, the bonding between the glass aggregate and cement paste is increased, leading to an enhancement in the concrete's strength [12]. On the other hand, the high replacement rates (above 60%) were observed to decrease the strength of concrete due to the poor crushing strength of glass and the higher water demand for concrete [4,13]. Despite the benefits of enhanced strength properties, the waste glass reacts with the alkalis present in the concrete matrix, causing the alkali-silica reaction (ASR) in concrete [14,15]. The ASR may affect the long-term performance of concrete due to the expansion of aggregates, causing cracking in concrete. Therefore, the substitution of fine aggregates with waste glass has durability issues and brings little economic advantage. Some research work has investigated ground waste glass powder as a supplementary cementitious material (SCM) in concrete and observed that the replacement of up to 20% of cement could enhance the strength properties [16,17]. The waste glass contains amorphous silica, which can undergo a pozzolanic

*Corresponding author. Email: saya.ramakrishnan@unisq.edu.au

reaction in the cementitious environment, thus improving the strength properties [18].

The amorphous silica (SiO_2) present in the waste glass could possess potential benefits in geopolymer concrete by undergoing a geopolymerization reaction in the presence of alkali activators. Geopolymer binder is identified as a sustainable alternative for Portland cement in concrete, where it can reduce the environmental issues associated with carbon dioxide (CO_2) emissions from cement manufacturing [19–21]. Geopolymer binders can be formulated using the silica and alumina rich waste byproducts such as fly ash, ground granulated blast furnace slag, metakaolin [22], waste colemanite [23], agro-industrial wastes [24], waste marble powder [25], etc. As per the author's best knowledge, only a few studies have investigated the possibility of incorporating waste glass in the geopolymer concrete as the precursor. For instance, Si et al. [26] reported that the mechanical properties and the microstructure characteristics were improved by introducing the glass powder at small dosages (5%–10% of the precursors). In another study, it was found that the addition of waste glass for up to 20% of the binder enhanced the mechanical properties of geopolymer concrete by 7% [27]. More recently, Jiang et al. [28] and Manikandan et al. [29] studied the effect of waste glass in geopolymer concrete and recommended it as a potential alternative to replace the depleting precursor sources of fly ash and slag in geopolymer concrete. Therefore, geopolymer concrete containing waste glass as a precursor could promote the recycling rate of glass for construction applications.

Despite the growing attention to recycling and sustainability in construction materials, conventional construction also operates at low efficiency with little or no adoption of automation technologies. The construction sector is a labor-intensive market involving large amounts of manual handling, logistics and waste generation. More recently, this sector has started to experience an unprecedented rate of disruption, thanks to digital construction and construction automation methods. The combination of these two technologies is expected to revolutionize the construction industry by significantly reducing the manual labor-intensive workforce and improving the efficiency of construction processes. In particular, 3D concrete printing (3DCP) has become an emerging digital construction method with its inherent merits of a reduced labor force, less resource consumption and waste generation, greater design freedom and improved worker safety [30–32]. 3DCP using extrusion-based technology allows the structures to be built as a layer-by-layer process using a digitally controlled nozzle [33,34].

The utilization of waste materials in 3DCP has gained significant interest in recent decades due to the sustainability merits and waste minimization in the construction industry. Various waste material sources, including construction and demolition waste [35,36], waste glass [37], and ground waste tyres [38] were studied as a partial substitution for aggregates in 3DCP. A limited studies have also investigated the utilization of waste materials as a cement replacement in printable concrete [39–41]. For example, Pasupathy et al. [42], Derya et al. [43], and Hau et al. [44] used the waste brick powder, marble dust, and recycled concrete powder respectively as a binder substitution in printable concrete. They found that the binder replacement with these waste materials has a significant reduction in the carbon footprint of printable concrete. These materials were also reported to enhance the rheological properties of printable concrete.

Although previous studies have explored waste glass powder as a supplementary cementitious material in conventional concrete and geopolymer systems, limited research has investigated its use as a primary precursor replacement in fly ash-slag-based geopolymer concrete specifically designed for 3D concrete printing (3DCP). This study addresses this gap by systematically evaluating the fresh rheological properties critical for printability, mechanical performance, and the post-fire behavior of 3D printed geopolymer concrete with varying WGP contents. By integrating waste glass into 3D printable geopolymer mixes, this study provides novel contributions to sustainable materials development aligned with digital construction technologies, advancing both waste valorization and additive manufacturing in construction.

Concerning that glass waste generation is steadily increasing, and it has great potential to be used as a precursor in geopolymer concrete, this study focuses on utilizing waste glass as a precursor in printable geopolymer concrete. For this purpose, the waste glass powder at different dosages of 0%, 15%, 30%, and 50% of precursors was incorporated into fly ash-slag-based geopolymer concrete and their fresh properties required for printable mixes were assessed along with the hardened properties. Besides, the geopolymer reaction rate with the waste glass dosage was evaluated using Fourier Transform Infrared Spectroscopy (FT-IR) analysis. Moreover, the published research studies suggest that the waste glass powder improves the performance of concrete when exposed to elevated temperatures. This is due to the melting and subsequent re-solidification of the waste glass powder within the concrete matrix, which aids in preserving the matrix integrity of the concrete [45]. Therefore, the elevated temperature performance of 3D printed samples was evaluated by assessing the strength properties and comparing them with the 3D printed samples without waste glass. The outcome of this study informs the effect of WGP as a substitution for the precursors in geopolymer 3DCP to address the pressing challenges of sustainability and waste management in the construction industry.

2. Methodology

2.1. Materials

The class F fly ash and ground granulated blast furnace slag (hereafter called slag) used in this study were supplied by Cement Australia and Independent Cement and Lime Pty Ltd., Australia, respectively. Both fly ash and slag comply with the Australian standard AS 3582.1 [46]. The waste glass powder (WGP) was supplied by Vortexis,

Australia. The median diameter (D50) of WGP, as provided by the supplier, was 20.5 µm. Table 1 presents the chemical composition of the fly ash and slag, and WGP, which was derived from X-ray fluorescence spectrometry (XRF) analysis. The alkali activator is sodium metasilicate (Na_2SiO_3) anhydrous powder ($SiO_2/Na_2O = 1.0$) purchased from Redox Pty Ltd., Australia.

Two types of graded silica sand (S_1 and S_2) with a median diameter (D50) of 172 µm (S_1) and 498 µm (S_2) were used to develop the 3D printable geopolymer mixes, respectively. Furthermore, a small dosage of sucrose powder was used in the geopolymer as a retarder to increase the open time of geopolymer concrete, as indicated by [42].

2.2. Characterization of waste glass powder

Table 1 shows that WGP mainly consists of three elements: SiO_2 (62.31%), Na_2O (10.5%), and CaO (9.78%). It should be noted that the glass is mainly comprised of SiO_2; however, the presence of Na_2O and CaO oxides could be due to the presence of soda lime-type glass in the waste [47]. The crystalline phases in the WGP were investigated using X-ray diffraction (XRD) analysis, and the test results are shown in Figure 1(a). It can be inferred from the test results that while the majority of the WGP is composed of quartz (SiO_2), other components such as albite ($NaAlSi_3O_8$), mullite ($Al_6Si_2O_{13}$), and hematite (Fe_2O_3) were also detected. Moreover, the XRD graph exhibits a broad amorphous shoulder between the broad bands of 20° and 40°, which is attributed to the glassy or amorphous phase of the glass powder. The amorphous content in the WGP was determined as 90.1%, which suggests that the glass powder has high amorphous silica content.

Figure 1(b) illustrates the FT-IR test results of WGP. The FT-IR spectrum indicates the main broadband at 1010 cm^{-1}, representing the asymmetric stretching vibration of Si–O–T linkages (T = Si or Al). In addition, a small intensity peak observed at the band of 770 cm^{-1} corresponds to the symmetric stretching vibration of Si–O–T linkages (T = Si or Al). Additionally, there is a small peak detected at the wave number of 1430 cm^{-1}, which is related to the stretching vibration mode of O-C-O (carbonate component - CO_3^{2-}) [48].

2.3. Sample preparation and 3DCP process

Table 2 shows the mix details of the materials used to prepare the 3D printable geopolymer concrete. The WGP is incorporated at three different dosages of 15%, 30%, and 50% of precursors to assess the effect of different WGP dosages on the printability properties of geopolymer concrete. These dosages were chosen as part of a preliminary optimization strategy to assess the impact of increasing WGP content on geopolymer properties. The 15%, 30%, and 50% replacements allow for comparative analysis to determine the most effective and sustainable utilization level of WGP. The control mix, without the WGP content, was also prepared to serve as the benchmark for the study. The preparation process of geopolymer mixes is as follows. Initially, the dry components of the mix, including slag, fly ash, WGP, two types of sand, Na_2SiO_3, and the retarder, were added in a Hobart mixer, and the mixing

Table 1. XRF Test results of raw materials.

	SiO_2 (%)	Al_2O_3 (%)	CaO (%)	Fe_2O_3 (%)	K_2O (%)	MgO (%)	Na_2O (%)	P_2O_5 (%)	SO_3 (%)	TiO_2 (%)	MnO (%)	LOI[a] (%)
Slag	33.5	12.53	41.83	0.29	0.42	5.96	0.2	0.006	4.02	0.68	0.27	0.24
Fly ash	53.73	26.33	5.9	8.45	0.732	1.14	0.26	0.42	0.277	1.52	0.13	1.18
WGP	62.31	3.93	9.78	4.64	0.465	1.61	10.5	0.12	0.357	0.19	0.1	4.58

[a]LOI means loss of ignition.

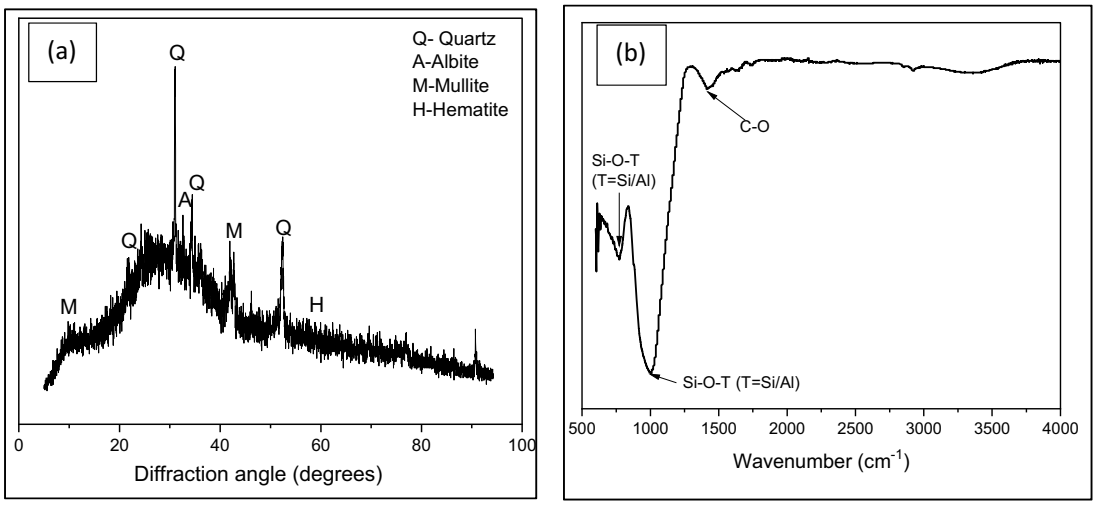

Figure 1. (a) XRD and (b) FTIR test results of WGP.

Table 2. Mix composition of materials.

Mix ID	Slag	Fly ash	WGP	Sand		Activator	Water	Retarder
				'S$_1$'	'S$_2$'			
50S/50F	0.5	0.5	–	0.5	1.0	0.1	0.4	0.01
50S/35F/15G	0.5	0.35	0.15	0.5	1.0	0.1	0.4	0.01
50S/20F/30G	0.5	0.2	0.3	0.5	1.0	0.1	0.42	0.01
50S/0F/50G	0.5	–	0.5	0.5	1.0	0.1	0.42	0.01

Figure 2. Gantry type 3D printer used for printing purposes.

was conducted for 3 min to ensure the uniform blending of dry materials. After that, 85% of the required water content was slowly added to the dry components, and the mixing was continued for 10 min. Then, the remaining water content of the total required water was added to the mixture, and the mixing was conducted for another 5 min. The reason for adding the water as two separate phases is to avoid the workability loss of the mix during the dissolution and to allow enough time to dissolve the metasilicate, as reported previously [42].

The 3DCP process was conducted using a three-axis gantry-type 3D printer, as shown in Figure 2. The printer has a maximum working space of 1800 mm (L) × 1600 mm (W) × 1800 mm (H). As shown in Figure 2, an auger extruder was attached to the three-axis rail system, and the navigation of the extruder movement was controlled by a customized computer program in the printer software interface. The extruder has an open inlet at the top for the feeder, and it has a circular outlet with a diameter of 30 mm at the bottom for the print. For this study, the samples were printed layer by layer at a speed of 10 mm/s, and the dimensions of each layer are 30 mm (W) × 300 mm (L) × 20 mm (H). After completing the printing, the freshly printed samples were covered with plastic film to prevent moisture evaporation from the printed samples. After 24 h, the samples were removed from the platform and placed in a sealed container at the ambient temperature until the test date. Moreover, the fresh geopolymer mixes were also cast in a $25 \times 25 \times 25\,mm^3$ cubical mold, and the curing process was the same as the printed specimens to compare the properties of the printed samples with the mold-cast specimens.

3. Experimental program

3.1. Reaction rates of geopolymerization with waste glass powder

The geopolymerization reaction rate and the nano structural formation of mixes with varying WGP dosage were evaluated by Fourier Transform Infrared Spectroscopy (FTIR) analysis. To conduct the FTIR, a Nicolet™ FTIR Spectrometer was employed. During the test, the transmittance spectra were collected in the range of 600 cm^{-1} to 4000 cm^{-1} with a scan rate of 32 scans per sample at a resolution of 4 cm^{-1}. The reading was collected after 0 min, 30 min, 1, h, 2 h, 1 day, and 28 days to assess the geopolymerization reaction rates with time. For this test, geopolymer mixes were prepared without sand to eliminate the peaks detected for sand during the measurements.

3.2. Flowability of fresh printable concrete

The flowability of the fresh mix was measured using a flow table test, as per ASTM C1437. A standard flow cone with an internal diameter of 100 mm at the bottom and 70 mm at the top with a height of 60 mm, was employed to conduct the flowability test. During the measurement, the fresh mix was filled into the flow cone as two layers, and then the cone was lifted. Consequently, the spread diameter was measured in two perpendicular directions, and the average flow diameter was determined. Following this, the flow table was dropped 25 times, and the final spread diameter was measured in two perpendicular directions, and the average flow diameter was determined.

3.3. Effect of waste glass powder on rheological properties

The rheological properties of fresh printable mixes are crucial to ensure the mixes have good pumpability and extrudability properties. For this purpose, a Viskomat XL rheometer with a six-blade vane probe setup was employed to measure the rheological properties. The dimensions of the vane probe are 34.5 mm in radius and 69 mm in height. The following rheological properties were assessed for the mixes.

3.3.1. Viscosity recovery and dynamic behavior of fresh mixes

Thixotropy refers to the ability to recover to the original viscosity after being subjected to a shearing process [49]. Shear-thinning materials such as concrete exhibit a decrease in apparent viscosity when subjected to a transition from low to high shear rates. Thus, it is critical to ensure that the concrete mix can recover its viscosity following high-shear mixing and return to its initial state at a low-shearing rate. During the 3D concrete printing process, there is an initial low shearing rate during pumping, followed by a high shearing stage during extrusion, which is succeeded by a low shearing rate during placement. It is important to ensure that the fresh concrete recovers its viscosity when transitioning from extrusion to placement (ie high shear to low shear), and a viscosity recovery test is generally carried out to assess this criterion. Figure 3 shows the protocol used to evaluate the viscosity recovery of the fresh mixes. Here, the apparent viscosity of the fresh mixes was determined at three stages. In the first stage, the mix was sheared at the low rate of 0.01 s^{-1} for 60 s to represent the pumping process before feeding into the extruder. In the second stage, the mix is sheared at the maximum rate of 13 s^{-1} for 30 s to represent the extrusion process of concrete. In the third stage, the low shearing rate (0.01 s^{-1}) was continued again to resemble the placement of concrete following the extrusion process. The recovered viscosity at this stage determines the ability of the material to re-flocculate after shearing, which subsequently reveals the shape retention ability of printed layers.

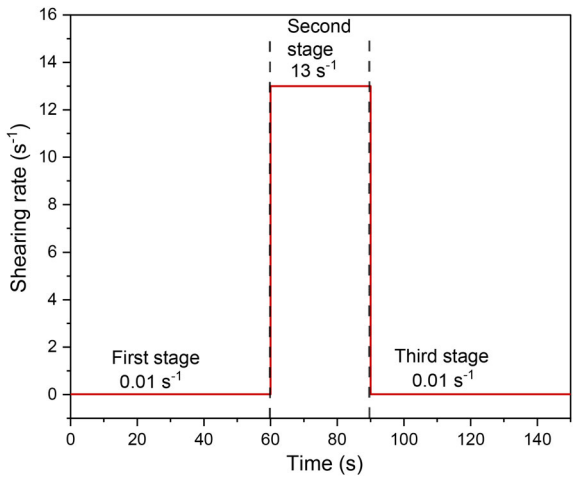

Figure 3. Rheological testing protocols for viscosity recovery measurements (reproduced from [42]).

The dynamic yield stress and plastic viscosity were determined by using a flow curve test using the protocol provided in Figure 4. As shown in Figure 4(a), the shear rate was increased from 0 to 80 RPM over 100 s, followed by an immediate decrease from 80 to 0 RPM over the next 100 s. Fresh concrete usually exhibits non-Newtonian behavior and therefore, the Bingham model can be used to determine the dynamic yield stress and plastic viscosity. The dynamic yield stress is determined by fitting the curve to a Bingham model and corresponds to the point where the line intersects the vertical axis. Plastic viscosity, on the other hand, represents the internal friction between the solid and liquid phases in concrete when the gel-like structure within the fluid is in a state of dynamic balance between destruction and restoration. It is determined by the slope of the fitted line in the Bingham model. The data in this study were fitted using the following Bingham model.

$$\tau = \tau_o + \mu\gamma \tag{1}$$

where τ is the shear stress, τ_0 is the yield stress, μ is the plastic viscosity, and γ is the shear rate.

3.3.2. Evolution of static yield stress with time

The productivity of 3DCP is largely governed by the buildability of printable concrete, which is referred to as the ability to print layer-by-layer without the excessive deformation or collapse of the layers. Buildability is one of the critical performance indicators in 3DCP, and it is important to assess the effect of WGP-incorporated geopolymers on the buildability performance. This is generally assessed by measuring the static yield stress development of concrete with time. In this study, a slow penetrometer was employed to assess the yield stress development of the fresh concrete mixes with time. Figure 5 illustrates the experimental setup for the penetrometer test used in this study. A 20 mm diameter penetrating needle with a 30 mm height conical head is attached to the load cell, which is installed in a Mechanical Testing Systems (MTS) machine. The accuracy of the load measurement is 0.1 N. The fresh concrete was prepared and filled into a cup, and the penetration of the needle through the fresh mix was conducted at the rate of 30 mm/h. Based on the penetration resistance measurements, the yield strength values were determined by using the following equation [50]:

$$T_0 = \frac{F}{\pi R\sqrt{R^2 + h^2}} \tag{2}$$

where F is the penetration resistance (in N), and R and h denote the radius and height in mm of the needle cone respectively.

3.4. Apparent volume of permeable voids (AVPV) and bulk density assessment

The bulk density and AVPV of 3D-printed concrete were determined as per ASTM C642. For this test,

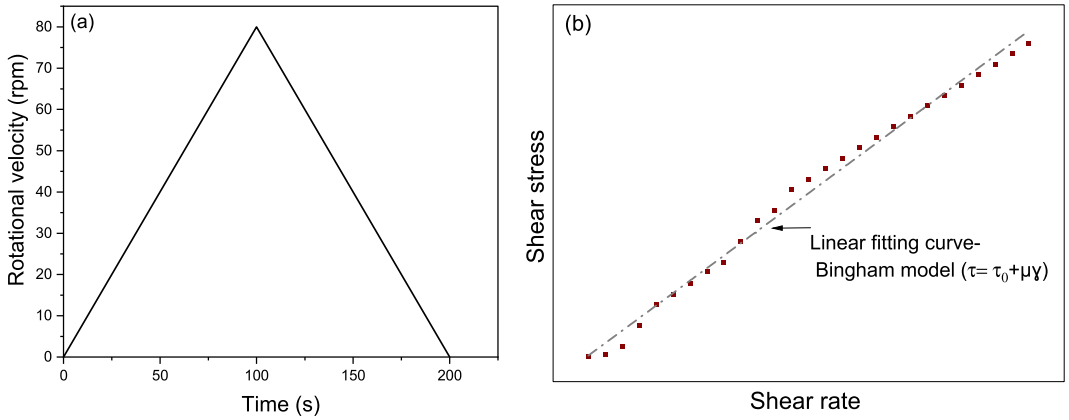

Figure 4. Rheological testing protocols for dynamic yield stress and plastic viscosity measurement.

Figure 5. Experimental setup for static yield strength measurement.

$30 \times 30 \times 30\,mm^3$ samples were extracted from the 3D-printed filaments. Initially, the samples were subjected to oven-drying at 105 °C for 24 h, and the oven-dried weight of the samples (D in g) were recorded. The samples were then immersed in water for 24 h and then submerged in boiling water for 6 h. The weight measurement after saturation and boiling was measured (B in g). The suspended weight of the samples was then measured and recorded as S (in g). The precision of the balance used for these measurements is 0.01 g. Using the obtained weight measurements, the bulk density (BD) in kg/m^3 and the AVPV (%) values were calculated as follows.

$$BD = \frac{D}{B - S} \times 1000 \quad (3)$$

$$APVP\ (\%) = \frac{B - D}{B - S} \times 100\% \quad (4)$$

3.5. Compressive strength properties of concrete

The compressive strength of 3D-printed concrete was evaluated by measuring the strength properties in three different directions: longitudinal, lateral, and perpendicular. Figure 6 provides a schematic diagram of the compressive strength test specimens in the three testing directions to evaluate the anisotropic behavior of the printed samples. Cube specimens with the dimensions of $30 \times 30 \times 30\,mm^3$ were extracted from the printed filaments and subjected to compressive strength testing using a Universal Mechanical Testing System (MTS) at 7 days and 28 days after printing. The MTS had a maximum load capacity of 300 kN and a precision of 0.01 kN. Three designated samples were tested in each direction, and the average and standard deviation of the results were reported. In addition, the compressive strength of the mold-cast specimens was also determined to assess the effect of printing compared to the conventional casting method. For this purpose, cubic mold cast specimens with dimensions of $25 \times 25 \times 25\,mm^3$ was tested after 7 and 28 days of the cast period. The testing method is the same as the one used for the 3D-printed samples described above.

3.6. Elevated temperature performance of 3D printed samples

To assess the heat resistance of 3D-printed geopolymer concrete incorporating WGP at elevated temperatures, the printed samples were subjected to two distinct temperatures: 400 °C and 600 °C. An electric muffle furnace with a maximum working temperature of 1100 °C was employed for this purpose. After exposing the samples to elevated temperatures for a duration of 1 h, the samples were allowed to cool down before conducting compressive strength tests. The compressive strength measurements were determined using the procedure mentioned in Section 3.5. Here, the compressive strength only in the perpendicular direction of the printed samples was assessed.

3.7. Micro-morphology analysis

The micro-morphology analysis of the 3D printed samples was conducted using a scanning electron microscope (SEM, ZEISS Supra 40 VP). The 10 mm slice specimens were derived from the 3D printed specimens. Prior to the test, all the samples were coated with a 15 nm gold coating using a K975X vacuum coating system and the SEM images were then captured using an accelerated voltage of 5 kV and a working distance (WD) of 13–18 mm.

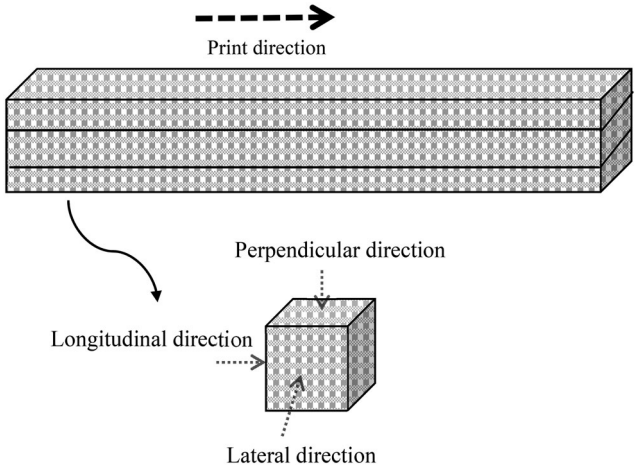

Figure 6. Schematic diagram of three different printing directions for the compressive strength test.

4. Results and discussion

4.1. Reaction rates of geopolymerization with waste glass

Figure 7(a–d) illustrates the FT-IR test results of mixes with the age of concrete to assess the reaction rate with the WGP content in the mixes. It can be observed from the graphs that the main band related to the Si–O and Al–O bonds from the geopolymerization process is observed in the range of 915–940 cm^{-1} for all the types of mixtures [51]. With the increasing age of concrete, the wavenumber of this peak shifts toward the right, indicating the high degree of polymerization due to SiO_2 cross-linking [52]. For instance, the main peaks for the 50S/35F/15G mix design formed at the wavenumber of 916 cm^{-1} at 0 min, which has shifted to 939 cm^{-1} after one day. Figure 7(e) depicts the FTIR spectra of geopolymer mixes after 28 days of age. The results demonstrated that the main band of geopolymerization reaction (Si–O and Al–O bonds) is further shifted toward the right due to the high amount of silica participation as geopolymerization gel, due to a higher degree of polymerization with the time of curing [52].

According to Figure 7(e), The control type 50S/50F mix displayed the main peak at the wavenumber of 965 cm^{-1}, which represents the asymmetric stretching vibrations of Si–O and Al–O bonds, showing the main geopolymerization reaction product [53]. On the other hand, major peaks identified for 50S/35F/15G, 50S/20F/30G, and 50S/0F/50G were at the wave numbers of 958 cm^{-1}, 948 cm^{-1} and 929 cm^{-1}, respectively. This indicates that the increasing dosage of WGP leads to the shift of peaks associated with the Si–O and Al–O bonds toward the left. This was also observed in the initial stage as well (Figure 7(a–d)). The shift of the major band to low wavenumbers is attributed to the increasing Si/Al ratio with the replacement of WGP [54]. This is primarily due to the increased SiO_2 and reduced Al_2O_3 with the WGP content.

Moreover, there are two additional minor peaks observed in all mixes at the wavenumber of 690 cm^{-1} and 873 cm^{-1}, which are related to the symmetric stretching vibration of Si–O and Si–O–Si, and O–C–O bonds within the CO_3^{2-} groups, respectively [55]. In addition, the presence of prominent peaks around 3446 cm^{-1} and 1652 cm^{-1} indicates the occurrence of asymmetric stretching and bending vibrations, respectively, in the O–H group of the bound water within the products [19]. These peaks signify that the free water present in the matrix undergoes a gradual transformation into bound water through the hydration reaction. Besides, the peak observed at approximately 1440 cm^{-1} corresponds to the asymmetric stretching mode of O–C–O bonds within the CO_3^{2-} groups formed by the reaction of alkali metal hydroxides with atmospheric CO_2 or the presence of CO_3^{2-} in the raw WGP, which has been identified from FT-IR spectra of WGP. These peaks were also recognized in all types of mixes.

4.2. Flow and setting time measurements of fresh mix

Figure 8 illustrates the impact of varying levels of WGP substitution on the slump and slump flow measurements of 3D printable geopolymer concrete mixes. The slump values of all the mixes, regardless of the WGP content, are approximately 100 mm, indicating that these mixes are zero-slump in nature. This is required for the shape retention ability of 3D-printed concrete. On the other hand, the slump flow value slightly increases with the WGP dosage. Compared to the control mix, the flow diameter of the 50S/0F/50G mixture increased by 10%. It should be noted that the slump-flow results of fresh concrete mixes are related to the dynamic yield stress and pumpability in 3D concrete printing [56]. As observed in the following section, the dynamic yield stress and plastic viscosity are reduced with the increasing WGP in the mix, which can be associated with the slump flow measurements. Thixotropy is a fluid behavior characterized by reversible changes in viscosity caused by flocculation at rest and deflocculation after shearing [57]. In this study, the slump measurements of all the mixtures were the same, regardless of the WGP content in the mix. However,

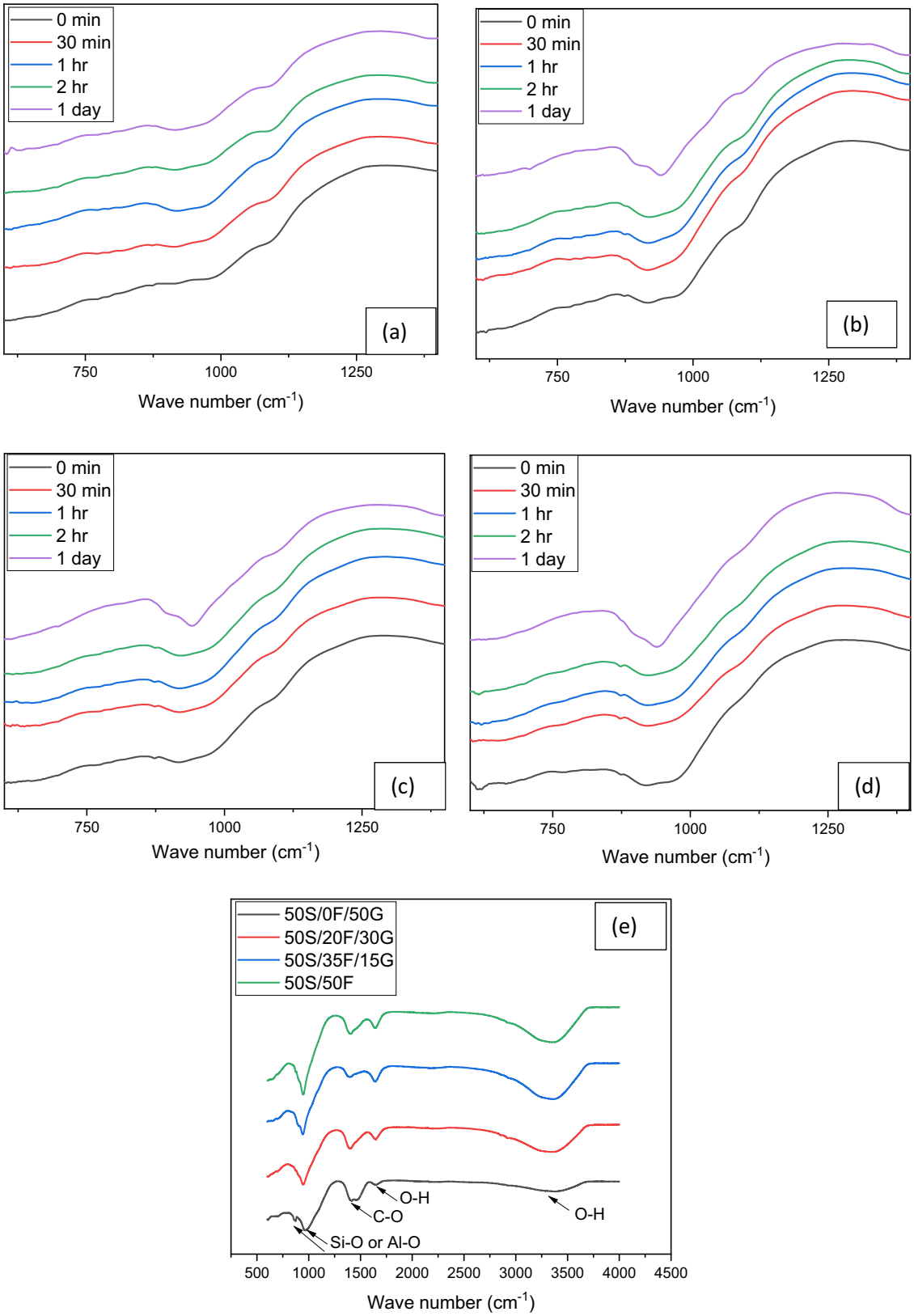

Figure 7. FTIR analysis of different geopolymer mixes with varying WGP content; (a) 50S/50F; (b) 50S/35F/15G; (c) 50S/20F/30G; and (d) 50S/0F/50G.

the flow measurements increased with the WGP after being subjected to drops in the flow table. This indicates that the thixotropy of concrete is increased with the WGP content in the printable mix, and this was also confirmed with the viscosity recovery measurements as described in the next section.

Based on the slump flow measurements, the printability of 3D printing can be determined. Tay et al. [56]

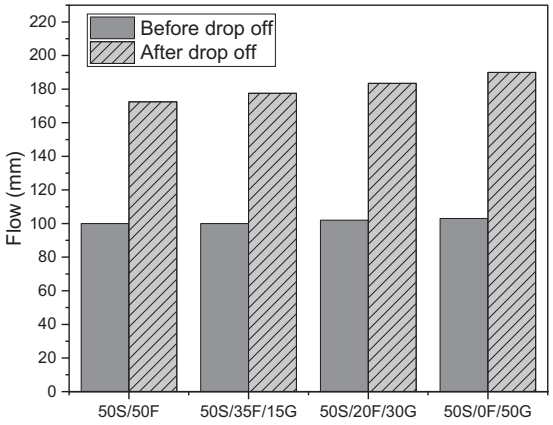

Figure 8. Flow measurements of 3D printable mixes with varying WGP contents.

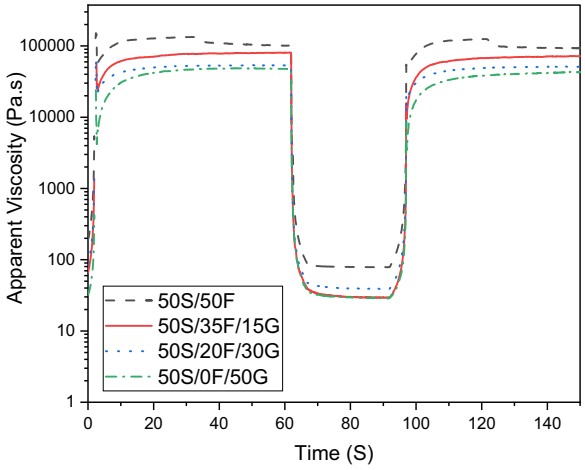

Figure 9. Viscosity recovery measurements of 3D printable mixes with varying WGP contents.

Table 3. Setting time measurements of 3D printable mixes with varying WGP contents.

Mix type	Initial setting time (min)	Final setting time (min)
50S/50F	55	70
50S/35F/15G	62	75
50S/20F/30G	70	84
50S/0F/50G	77	92

observed that the slump flow values between 150 mm and 190 mm give a smooth surface and high buildability. The slump flow values of the current study are in this range and can be considered as the printable region for all types of mixtures. However, to understand the rheological properties with the addition of WGP in the mixes, a detailed rheological properties analysis was conducted as provided in the following section.

The initial and final setting times of 3D concrete printable mixes with WGP content were also determined using a Vicat apparatus and the results are provided in Table 3. As can be seen in Table 3, the initial and final setting times are increased with the WGP content. The initial and final setting times of the control mix were 55 min and 70 min, respectively. The corresponding setting time values observed for the 50S/0F/50G type mix were 77 min and 92 min, respectively. An increase in the setting time with WGP content is attributed to the slow dissolution and the reduced reaction rates of WGP compared to fly ash particles [58]. As evident from the static yield stress measurements provided below, the final static yield stress values decrease with the addition of WGP in the mix, indicating the slow reactivity of the geopolymer concrete with WGP.

4.3. Rheological behaviors of 3D printable concrete with WGP

4.3.1. Viscosity recovery

Figure 9 illustrates the apparent viscosity recovery results of the various 3D printable mixtures as measured by the rheological protocol provided in Section 3.3.1. The protocol measures the viscosity at three stages of low, high, and again low shearing rates. As can be seen in Figure 9, at the initial stage of low shear rates, high apparent viscosity was observed for all mixes, and the viscosity values decreased at the high shear rates in stage 2. After that, the viscosity values increased again to reach the initial viscosity values at the low shearing rate, indicating the shear-thinning behavior of concrete. Here, all the mixes, irrespective of the WGP content, showed good recovery rates. The recovery rate observed for the 50S/50F, 50S/35F/15G, 50S/20F/30G, and 50S/0F/50G were 90%, 89%, 93%, and 90%, respectively. However, it is interesting to note that the apparent viscosity values are decreasing with the increasing WGP in the mixes at both low and higher shearing rates. Apparent viscosity is typically used to represent the internal friction between particles in the mix [59]. The decreasing trend of the apparent viscosity with the increasing WGP content indicates reduced friction between particles, which could be due to the smooth and glassy surface of the WGP powder [29]. However, further investigation is necessary to validate this observation.

Furthermore, the measured viscosity values in this study, ranging from approximately 10 to 100 Pa·s at low shear rates and 10,000 to 100,000 Pa·s at high shear rates, are consistent with those reported in prior studies on 3D-printable alkali-activated systems [60]. These values fall within the rheological thresholds identified as optimal for extrusion-based additive manufacturing, supporting both pumpability and buildability without excessive deformation or blockage [60].

Furthermore, the FTIR findings support the rheological behavior observed in this study. The lower reactivity of WGP, evidenced by the delayed and lower wavenumber of Si–O and Al–O peaks, corresponds to a slower formation of geopolymer gel and reduced structural build-up. This demonstrates as lower static yield stress values and higher flowability in fresh-state rheology. The weaker interparticle bonding inferred from FTIR spectra aligns with the reduced internal friction and

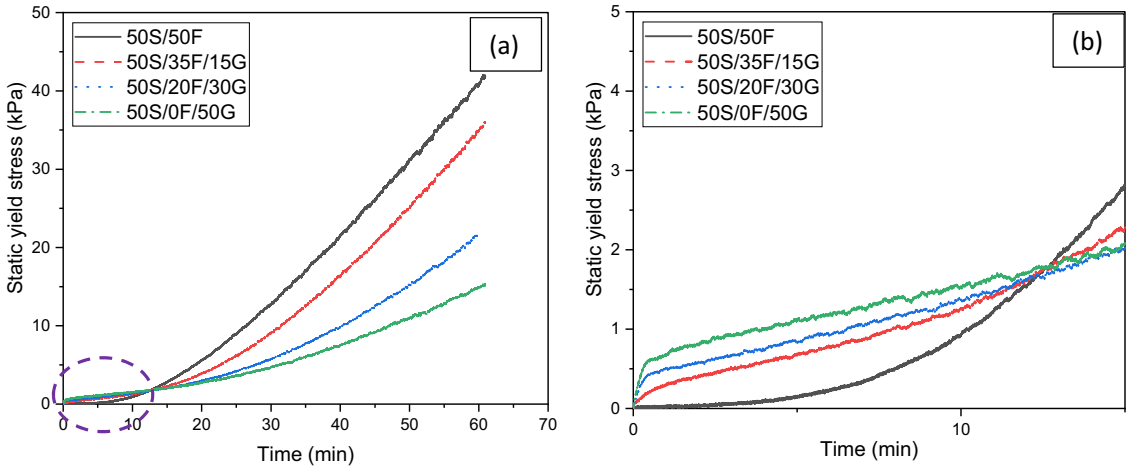

Figure 10. Yield strength development of 3D printable mixes with varying WGP contents.

apparent viscosity measured in high-WGP mixes, supporting the interpretation that the geopolymerization kinetics have a direct influence on rheological performance.

4.3.2. *Static yield stress development with WGP*

Figure 10 shows the yield strength growth with time for all the mixes. As can be seen, there are two different trends of static yield stress behaviors. Up to 15 mins, the static yield stress increases with the WGP content at any time. After 15 mins, it shows a reversed trend of decreasing static yield stress with the WGP content. For example, the yield strength values of 50S/50F were 40 kPa at 60 mins, whereas the corresponding yield strength values for 50S/35F/15G, 50S/20F/30G, and 50S/0F/50G were 34, 21, and 15 kPa, respectively. However, as shown in Figure 10(b), at 8 min, the static yield stress of 50S/50F, 50S/35F/15G, 50S/20F/30G, and 50S/0F/50G were 0.54, 1.02, 1.18, and 1.4 kPa, respectively. The reduced SYS development rates with the increasing WGP dosage are due to the reduced dissolution and reaction rates of WGP as reported in Section 4.1. This decrease in static yield stress after 15 mins indicates that the freshly printed layers may have a reduced capacity to support subsequent layers, potentially affecting buildability and shape stability during printing. Moreover, the static yield stress values observed in this study are slightly lower than those reported in previous studies [60,61], which may be attributed to differences in precursor fineness, activator concentration, and particle packing density. To enhance static yield stress and structural buildability, future mix optimization could consider using finer WGP particles, or introducing thixotropy-enhancing additives such as nano clay or rheology modifiers.

4.3.3. *Dynamic yield stress and plastic viscosity measurements*

Concrete materials should exhibit a low dynamic yield stress and plastic viscosity when subjected to pumping and extrusion, and they should demonstrate a high static yield stress and the ability to recover viscosity once shear

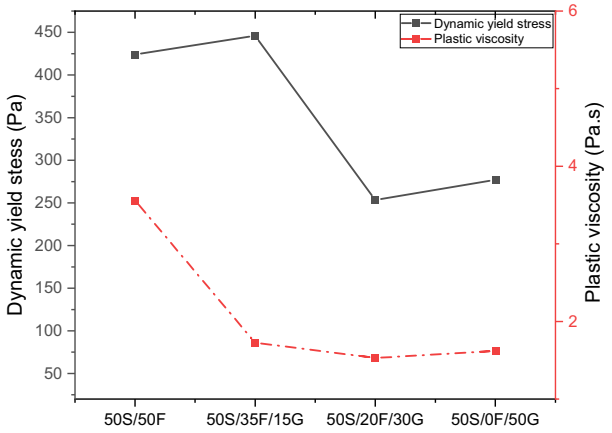

Figure 11. Dynamic yield stress and plastic viscosity of 3D printable mixes with varying WGP content.

forces are no longer applied after deposition [62]. The dynamic yield stress and the plastic viscosity of the geopolymer mix are determined from flow curves, as shown in Figure 11. As can be seen from Figure 11, the dynamic yield stress and the plastic viscosity values are decreased with the WGP content in the mix. For instance, the control mix showed the dynamic yield stress and plastic viscosity of 424 Pa and 3.56 Pa s, whereas the corresponding results of the 50S/0F/50G type mixes were 277.2 and 1.62 Pa s. This indicates that the addition of WGP in geopolymer 3D printing enhances the pumpability and flowability of the mix, which is beneficial for printing.

However, this improved flowability and pumpability with higher WGP content can contribute to increased porosity in the printed material, which correlates with the observed decrease in compressive strength and mechanical integrity. The higher porosity may result from weaker particle interactions and reduced geopolymerization due to the smooth surface and lower reactivity of WGP. Therefore, an optimization is required to balance printability benefits with mechanical performance to ensure both buildability and structural reliability.

The reduction in dynamic yield stress and plastic viscosity with increasing WGP content observed in this study

is consistent with trends reported in previous research. For instance, Sheng et al. [63] reported that dynamic yield stress decreased from approximately 241.94 Pa at 10% WGP to 178.52 Pa at 40% WGP. In their study, the plastic viscosity varied from 6.05 Pa.s to 6.03 Pa.s for 10% WGP and 40% WGP in geopolymer mix. In the present study, dynamic yield stress values ranged from 424 Pa (control mix) to 277.2 Pa (50% WGP), while plastic viscosity ranged from 3.56 Pa·s to 1.62 Pa·s. Despite differences in absolute values due to variations in geopolymer precursors, mix compositions, and measurement protocols, the overall trend remains comparable. These findings collectively indicate that increasing WGP content reduces the interparticle cohesion and internal resistance to flow, enhancing the pumpability and extrudability of 3D printable geopolymer mixtures.

4.4. Hardened properties of WGP incorporated 3D printed concrete

4.4.1. Compressive strength properties

Figure 12(a,b) illustrates the compressive strength of mold-cast and 3D printed samples at 7 days and 28 days, respectively. The compressive strength of WGP-incorporated concrete reduces with the increasing WGP dosage. Considering the mold cast specimens as an example, the compressive strength of the 50S/50F was 51.4 MPa at 28 days, whereas the strength properties of 50S/35F/15G, 50S/20F/30G, and 50S/0F/50G were reduced by 7.5%, 20.8%, and 30.7%, respectively. This indicates that the replacement of fly ash with WGP reduces the strength properties of geopolymer concrete. Similar behavior was also observed in the 3D-printed samples as well. For instance, the control 3D printed specimen showed the compressive strength of 41.5 MPa, 32.4, and 45.1 MPa for perpendicular, lateral, and longitudinal directions, respectively. However, the compressive strength in corresponding directions was reduced to 29.3, 21.4, and 31.1 MPa, respectively, for 50% WGP replacement level. The reduction of compressive strength in these directions was determined as 29%, 34%, and 31%, respectively. The reduction of the compressive strength with the substitution of WGP can be related to the variation in the Si/Al ratio in the geopolymer mix due to the high SiO_2 content in WGP [27]. As a result, a high WGP-containing mix resulted in low-crosslinked aluminosilicate materials, leading to reduced compressive strength properties [58]. Although a reduction in compressive strength is observed with increasing WGP replacement, this effect could potentially be reduced by increasing the fineness of WGP to enhance its reactivity and packing density, or by incorporating suitable chemical admixtures. Future work is recommended to explore these options to improve the strength performance of geopolymer systems incorporating WGP. Moreover, the reduction in compressive strength with increasing WGP content is also consistent with the FTIR observations discussed in Section 4.1. The leftward shift (toward lower wavenumber) of the main Si–O–T (T = Si or Al) bands in FTIR spectra with higher WGP dosage indicates an increased Si/Al ratio and a less cross-linked aluminosilicate network. This is an indication of lower gel compactness and weaker structural integrity, which correlates with the observed decline in compressive strength at higher WGP contents. Therefore, the FTIR analysis confirms that the reduced polymerization degree associated with high-WGP systems adversely impacts mechanical performance.

In addition, WGP could possibly alter the porosity/air voids variation in the matrix, which would affect the strength properties. To assess the porosity/air voids variation, the porosity analysis was conducted, and the results are provided in the following section.

The anisotropic behavior was observed for the compressive strength of printed specimens. The printed specimens displayed the highest compressive strength in the longitudinal direction, followed by the perpendicular direction, and the lowest strength values were observed for the lateral loading directions. This is primarily because the extrusion process aligns the material filaments along the printing direction, resulting in enhanced particle packing, compaction, and material continuity, which together increase strength in this direction. In contrast, the low strength in lateral directions is attributed to the presence of a weak interlayer [64]. Interfaces between printed layers represent potential weak zones due to limited chemical bonding and incomplete geopolymerization across the layer boundaries. Additionally, delays between layer

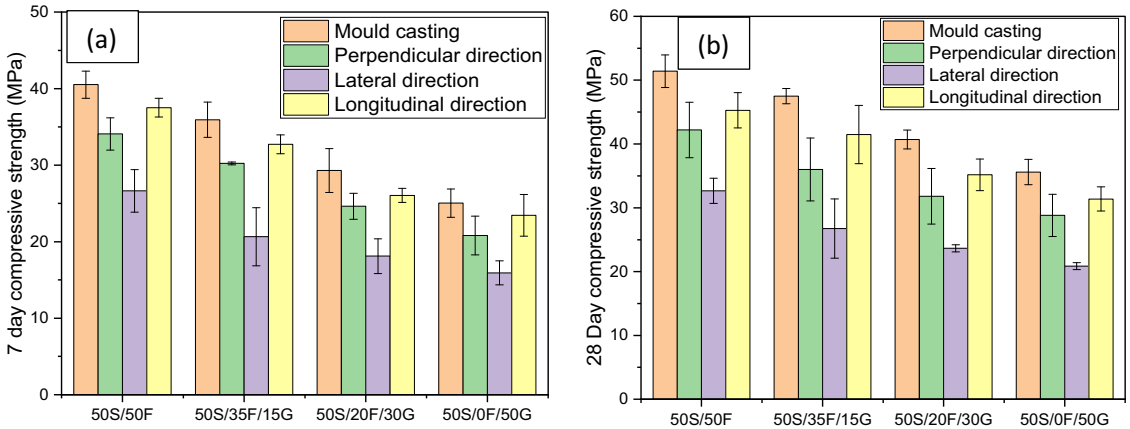

Figure 12. Compressive strength values with varying WGP contents at antistrophic directions: (a) 7 days and (b) 28 days.

depositions can cause surface drying and reducing adhesion. Mechanical interlocking at interfaces may also be insufficient, especially if printing parameters are not optimized, leading to increased interfacial voids and microcracks. These defects at the layer interfaces reduce the efficiency of load transfer perpendicular to the printing direction, causing reduced strength in the lateral directions.

Furthermore, the compressive strength of mold-cast specimens is higher than the printed specimens in all tested directions. As stated by past researchers [33,65,66], this is likely due to the presence of inherent voids formed during the printing process as a result of circular nozzles.

4.4.2. The apparent volume of permeable voids (AVPV) and bulk density

The apparent volume of permeable voids (AVPV) of mold cast and 3D printed samples is reported in Figure 13. The 3D printed samples showed higher AVPV than the mold cast specimens, regardless of the WGP content in the mixture. This behavior is attributed to the layer-by-layer fabrication process in 3DCP, compared to monolithic casting in mold-cast concrete. The layer-wise fabrication induces interlayer porosity in addition to the intralayer porosity in concrete. Furthermore, 3D printed specimens would not be subjected to compaction, whereas the cast specimens are mechanically vibrated during the casting process. These two factors cause the increased porosity in 3D printed specimens. Similar observations were also reported in past research studies [66–68].

The porosity variation between different types of mixtures indicated that the AVPV values are increased with the WGP content. The measured AVPV of 3D printed control mix was 13.2%, whereas the AVPV values of 50S/35F/15G, 50S/20F/30G, and 50S/0F/50G were 14.1%, 15.4%, and 17.9%, respectively. A similar observation has been reported by other researchers for the glass powder incorporated geopolymer concrete [69]. Figure 14 compares the surface morphology of the 3D printed filament for the 50S/50F and 50S/0F/50G types. It is evident that large voids are present in the 50S/0F/50G type concrete surface.

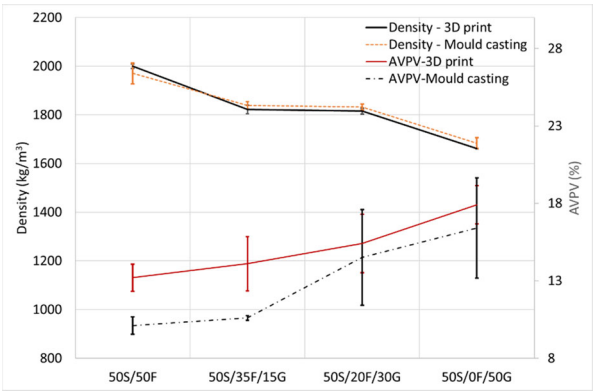

Figure 13. Bulk density and AVPV variation with WGP content; 3D printed and mold casting specimens.

The bulk density measurements of both 3D-printed and mold-cast concrete specimens are also provided in Figure 13. Regardless of the fabrication method (ie mold-cast or 3D-printed concrete), the density is reduced with increasing WGP in the mixes. The variation of the density with the WGP could be due to the increased porosity of WGP-incorporated specimens reducing the bulk density. In addition, the lower specific gravity of the WGP may also lead to the reduced density of the produced concrete.

Moreover, as porosity plays a critical role in the thermal stability of concrete, the increased AVPV values in WGP-rich mixes may initially suggest reduced fire resistance; however, the sintering behavior of WGP appears to offset this effect, as discussed in the following section.

4.5. Compressive strength of 3D printing concrete under elevated temperature

The compressive strengths of the 3D-printed concrete specimens with varying WGP dosage when exposed to elevated temperatures are given in Figure 15(a). The compressive strength loss percentages based on 28-day strength values are also calculated and provided in Figure 15(b). According to Figure 15(a), the compressive strength is reduced from 34.8 MPa to 25.1 MPa for the 50S/50FA mix when the exposure temperature is increased from 400 °C to 600 °C, whereas the corresponding reductions for 50S/0F/50G are from 24.1 MPa to 20.5 MPa. The control specimen showed the highest strength drop when the exposure temperature was increased to 600 °C. However, the rate of strength reduction reduces with the increasing WGP dosage, indicating that the WGP in geopolymer concrete had an excellent high-temperature resistance.

In addition to strength degradation, visual observations revealed notable physical changes in the specimens exposed to 600 °C. These include surface cracking, slight discoloration, and minor edge spalling in all specimens.

The above comparison suggests that the incorporation of WGP in geopolymer concrete enhances the structural integrity of concrete under fire. This can be attributed to the sintering process of glass powder associated with the melting and re-solidification of the WGP within the matrix. The sintering process allows transitioning from a ‘glass’ state to a ‘rubber’ state upon exposure to temperatures exceeding 600 °C [70]. This fire-resistant behavior makes WGP-based 3D printable concrete highly suitable for applications requiring both rapid fabrication and thermal stability, such as bushfire-resistant housing, fire shelters, and protective enclosures for critical infrastructure [70].

4.6. Microstructural analysis of 3D-printed concrete

The SEM analysis was carried out on geopolymer specimens containing WGP to visually examine the micromorphology characterization. Figure 16 illustrates the SEM images of 3D printed samples after 28 days of age. The visual observation of Figure 16(a) evident many spherical shaped particles in the control mix, which suggests the

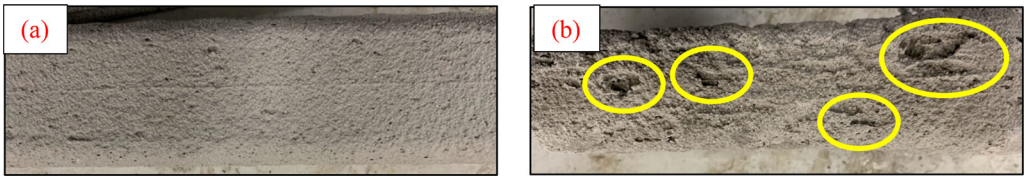

Figure 14. (a) Surface morphology of 50S/50F filament and (b) surface morphology of 50S/0F/50G filament.

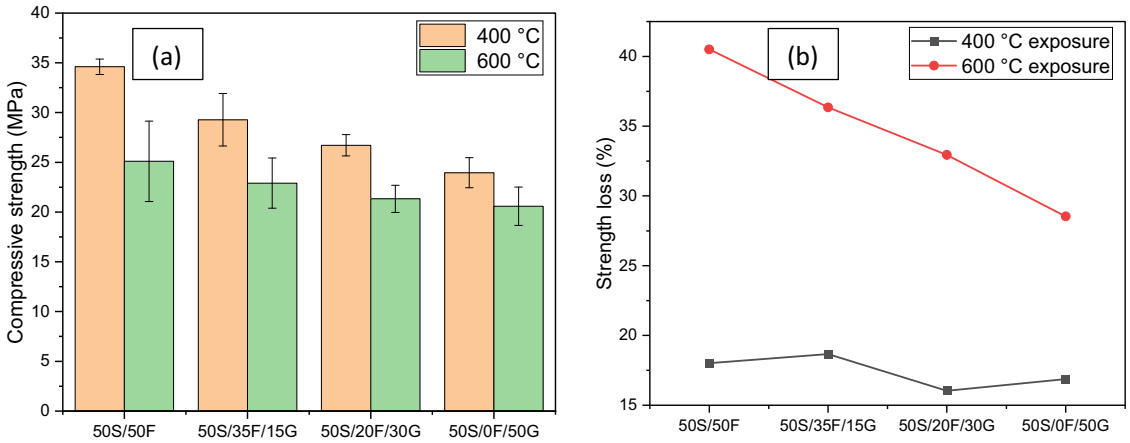

Figure 15. Compressive strength of 3D printed sample exposed in high temperature; (a) 400 °C and (b) 600 °C.

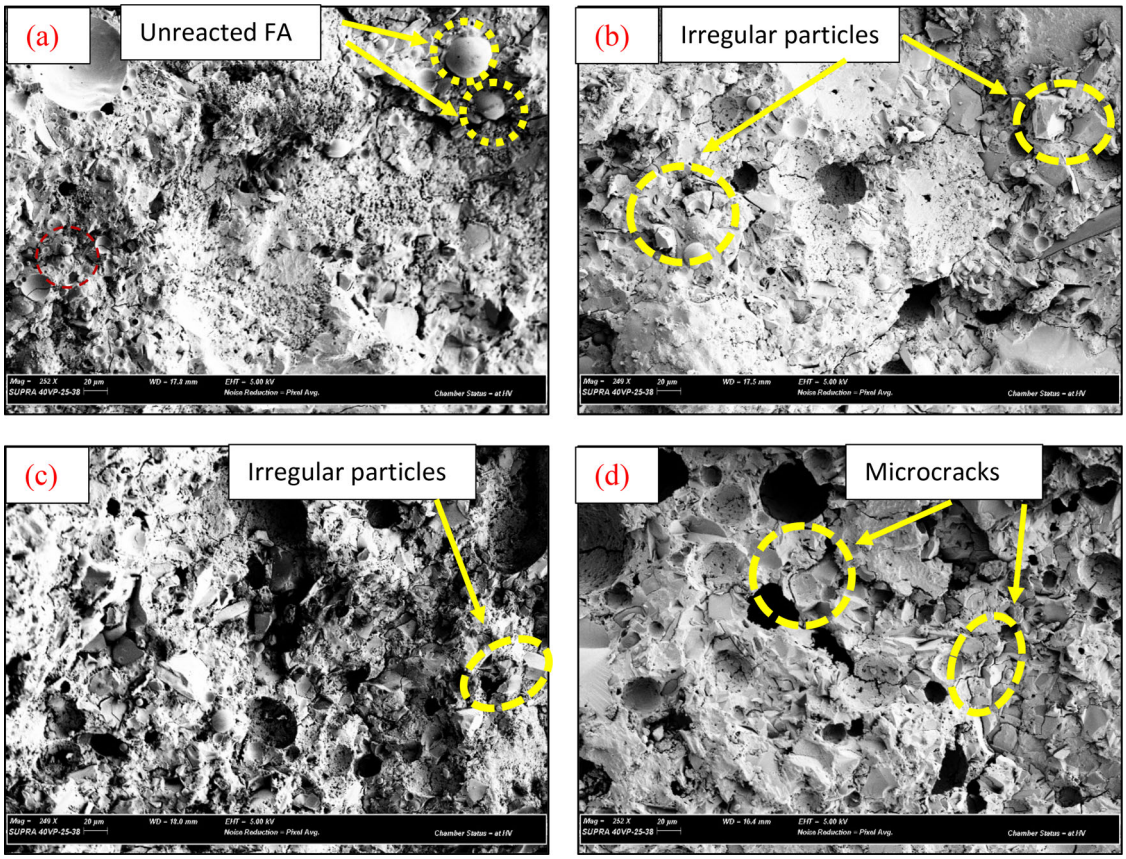

Figure 16. SEM images of (a) 50S/50F; (b) 50S/35F/15G; (c) 50S/20F/30G; and (d) 50S/0F/50G.

presence of unreacted fly ash particles. Similarly, Figure 16(b–d) shows the particles with irregular shapes, sharp edges, and smooth surfaces, which are unreacted WGP particles. The comparison of surface morphology between different samples also indicates an increase in voids and pores with the increasing WGP in the mix. In addition, multiple microcracks are visible in the 50S/0F/50G mix, which has the highest amount of waste glass in the mix. This behavior can be related to the compressive strength properties, where higher strength was observed for the control mix and the strength properties were reduced with the WGP content in the mix. This could be due to the

inadequate mechanical interlocking between the unreacted smooth glass particles and the gel matrix; thus, the densification of the matrix was reduced, leading to inferior mechanical properties [29,51]. Moreover, the ratio between Si and Al in the gel phases also significantly impacts the properties of geopolymers by altering the geopolymerization network [71]. As the Si/Al ratio increases with WGP, it leads to the creation of a low-crosslinked aluminosilicate network in the geopolymer matrix, which leads to a reduction in strength properties [58]. To get a more detailed understanding of the chemical composition and elemental distribution within the geopolymer matrix, future work is recommended to include Energy Dispersive Spectroscopy (EDS) analysis, which would enable quantification of elemental ratios such as Si and Al and facilitate a better correlation between microstructure and mechanical performance.

5. Conclusions

This study investigated the alkali activation of waste glass powder (WGP) in fly ash-slag-based geopolymer concrete for 3D concrete printing applications. WGP was used as the precursor in the geopolymer mixes and the effect of the WGP content on the fresh rheological, hardened properties and post-fire performance was assessed. Based on the experimental analysis, the following conclusions can be drawn.

- The WGP substitution for fly ash and slag precursors has a major impact on the geopolymerization rates as observed from the FTIR study. This is also reflected in the rheological properties of fresh printable concrete. The increase in WGP content reduces the apparent viscosity at both high and low shearing rates and increases the flowability of the mixes. On the other hand, the static yield strength decreases.
- The compressive strength of mold-cast and 3D-printed geopolymer concrete with high WGP content decreased in all three directions due to an increase in the Si/Al ratio in the mix. The maximum reduction in compressive strength was determined for 50% WGP replacement level as 29%, 34%, and 31% for perpendicular, lateral, and longitudinal directions, respectively. Nevertheless, the average compressive strength in all directions was above 20 MPa.
- The AVPV increased with an increase in WGP content in the geopolymer mix. The increased APVP can be correlated to the compressive strength loss of the specimens with the increasing WGP replacement levels.
- SEM images indicated that the homogeneity of the microstructure decreased with the increase in WGP content in the 3D printable mix, and this was attributed to the reduced reaction rates of WGP compared to other precursors. The high WGP content resulted in increased microcracks, pores, and voids due to the high porosity and low strength properties.

Therefore, these findings demonstrate the potential of WGP as a viable precursor for 3D printable geopolymer concrete, especially considering its beneficial effect on fresh concrete properties and fire resistance. However, to fully understand its practical application, further research is required to evaluate the long-term durability of WGP-based geopolymer concrete in real field conditions and to assess scalability and process optimization challenges for industrial-scale 3D printing.

Disclosure statement

No potential conflict of interest was reported by the author(s).

References

[1] Ting GHA, Tay YWD, Tan MJ. Experimental measurement on the effects of recycled glass cullets as aggregates for construction 3D printing. J Clean Prod. 2021; 300:126919. doi: 10.1016/j.jclepro.2021.126919.
[2] Australia E. National waste report; 2020. Available from: https://www.environment.gov.au/protection/waste/national-waste-reports/2020, 13 MArch 2024, Canberra, ACT: Australian Government
[3] Heriyanto F, Pahlevani, V, Sahajwalla. From waste glass to building materials – an innovative sustainable solution for waste glass. J Clean Prod. 2018;191:192–206. doi: 10.1016/j.jclepro.2018.04.214.
[4] Ismail ZZ, Al-Hashmi EA. Recycling of waste glass as a partial replacement for fine aggregate in concrete. Waste Manag. 2009;29(2):655–659. doi: 10.1016/j.wasman.2008.08.012.
[5] Mohajerani A, et al. Practical recycling applications of crushed waste glass in construction materials: a review. Constr Build Mater. 2017;156:443–467. doi: 10.1016/j.conbuildmat.2017.09.005.
[6] Jani Y, Hogland W. Waste glass in the production of cement and concrete – a review. J Environ Chem Eng. 2014;2(3):1767–1775. doi: 10.1016/j.jece.2014.03.016.
[7] Ahıskalı A, et al. Sustainable geopolymer foam concrete with recycled crumb rubber and dual fiber reinforcement of polypropylene and glass fibers: a comprehensive study. Constr Build Mater. 2025;474: 141137. doi: 10.1016/j.conbuildmat.2025.141137.
[8] Kaplan G, et al. The impact of natural and calcined zeolites on the mechanical and durability characteristics of glass fiber reinforced cement composites. Constr Build Mater. 2021;311:125336.
[9] Kılıç D, et al. Integration of reclaimed asphalt aggregates into glass fiber-reinforced alkali-activated composites: mechanical performance and durability. Constr Build Mater. 2025;458:139645. doi: 10.1016/j.conbuildmat.2024.139645.
[10] Benli A. Sustainable use of waste glass sand and waste glass powder in alkali-activated slag foam concretes: physico-mechanical, thermal insulation and durability characteristics. Constr Build Mater. 2024;438:137128. doi: 10.1016/j.conbuildmat.2024.137128.
[11] Gencel O, et al. Lightweight foam concrete containing expanded perlite and glass sand: physico-mechanical, durability, and insulation properties. Constr Build Mater. 2022; 320:126187. doi: 10.1016/j.conbuildmat.2021.126187.
[12] Ali EE, Al-Tersawy SH. Recycled glass as a partial replacement for fine aggregate in self compacting

concrete. Constr Build Mater. 2012;35:785–791. doi: 10.1016/j.conbuildmat.2012.04.117.
[13] de Castro S, de Brito J. Evaluation of the durability of concrete made with crushed glass aggregates. J Clean Prod. 2013;41:7–14. doi: 10.1016/j.jclepro.2012.09.021.
[14] Degirmenci N, Yilmaz A, Cakir OA. Utilization of waste glass as sand replacement in cement mortar. Indian Journal of Engineering & Materials Sciences, 18(4), 303-308.
[15] Kou SC, Poon CS. Properties of self-compacting concrete prepared with recycled glass aggregate. Cem Concr Compos. 2009;31(2):107–113. doi: 10.1016/j.cemconcomp.2008.12.002.
[16] Aliabdo AA, Abd Elmoaty AEM, Aboshama AY. Utilization of waste glass powder in the production of cement and concrete. Constr Build Mater. 2016;124:866–877. doi: 10.1016/j.conbuildmat.2016.08.016.
[17] Islam GMS, Rahman MH, Kazi N. Waste glass powder as partial replacement of cement for sustainable concrete practice. Int J Sustain Built Environ. 2017;6(1):37–44. doi: 10.1016/j.ijsbe.2016.10.005.
[18] Matos AM, Sousa-Coutinho J. Durability of mortar using waste glass powder as cement replacement. Constr Build Mater. 2012;36:205–215. doi: 10.1016/j.conbuildmat.2012.04.027.
[19] Pasupathy K, Ramakrishnan S, Sanjayan J. Effect of hydrophobic surface-modified fine aggregates on efflorescence control in geopolymer. Cem Concr Compos. 2022;126:104337. doi: 10.1016/j.cemconcomp.2021.104337.
[20] Pasupathy K, Ramakrishnan S, Sanjayan J. Enhancing the chemical foaming process using superplasticizer in aerated geopolymer concrete. Constr Build Mater. 2022;324:126535. doi: 10.1016/j.conbuildmat.2022.126535.
[21] Singh RJ, Raut A. Insulation effects of a roof system developed from waste-incorporated geopolymer concrete. Iran J Sci Technol Trans Civil Eng. 2023;47(6):3259–3276. doi: 10.1007/s40996-023-01119-5.
[22] Arslan S, et al. Sustainable use of silica fume and metakaolin in slag/fly ash-based self-compacting geopolymer composites: fresh, physico-mechanical and durability properties. Sustain Chem Pharm. 2024;38:101512. doi: 10.1016/j.scp.2024.101512.
[23] Alcan HG, et al. Effective utilization of silica fume and waste colemanite in eco-sustainable prepacked geopolymers. Constr Build Mater. 2024;457:139438. doi: 10.1016/j.conbuildmat.2024.139438.
[24] Raut AN, et al. Effects of agro-industrial by-products as alumina-silicate source on the mechanical and thermal properties of fly ash based-alkali activated binder. Case Stud Constr Mater. 2023;18:e02070. doi: 10.1016/j.cscm.2023.e02070.
[25] Bayrak B, et al. Recycling of waste marble powder and waste colemanite in ternary-blended green geopolymer composites: mechanical, durability and microstructural properties. J Build Eng. 2023;73:106661. doi: 10.1016/j.jobe.2023.106661.
[26] Si R, et al. Mechanical property, nanopore structure and drying shrinkage of metakaolin-based geopolymer with waste glass powder. J Clean Prod. 2020;242:118502. doi: 10.1016/j.jclepro.2019.118502.
[27] Jiang X, et al. Influence of waste glass powder on the physico-mechanical properties and microstructures of fly ash-based geopolymer paste after exposure to high temperatures. Constr Build Mater. 2020;262:120579. doi: 10.1016/j.conbuildmat.2020.120579.
[28] Jiang X, et al. Influence of size effect on the properties of slag and waste glass-based geopolymer paste. J Clean Prod. 2023;383:135428. doi: 10.1016/j.jclepro.2022.135428.
[29] Manikandan P, Vasugi V. Potential utilization of waste glass powder as a precursor material in synthesizing ecofriendly ternary blended geopolymer matrix. J Clean Prod. 2022;355:131860. doi: 10.1016/j.jclepro.2022.131860.
[30] Zhang Y, et al. Rheological and harden properties of the high-thixotropy 3D printing concrete. Constr Build Mater. 2019;201:278–285. doi: 10.1016/j.conbuildmat.2018.12.061.
[31] Wu P, Wang J, Wang X. A critical review of the use of 3-D printing in the construction industry. Autom Constr. 2016;68:21–31. doi: 10.1016/j.autcon.2016.04.005.
[32] Nguyen-Van V, et al. Modelling of 3D concrete printing process: a perspective on material and structural simulations. Addit Manuf. 2023;61:103333. doi: 10.1016/j.addma.2022.103333.
[33] Ramakrishnan S, et al. Concrete 3D printing of lightweight elements using hollow-core extrusion of filaments. Cem Concr Compos. 2021;123:104220. doi: 10.1016/j.cemconcomp.2021.104220.
[34] Boddepalli U, Panda B, Ranjani Gandhi IS. Rheology and printability of Portland cement based materials: a review. J Sustain Cem Based Mater. 2023;12(7):789–807. doi: 10.1080/21650373.2022.2119620.
[35] Wu Y, et al. Study on the rheology and buildability of 3D printed concrete with recycled coarse aggregates. J Build Eng. 2021;42:103030. doi: 10.1016/j.jobe.2021.103030.
[36] Zhang C, et al. Printability and pore structure of 3D printing low carbon concrete using recycled clay brick powder with various particle features. J Sustain Cem Based Mater. 2023;12(7):808–817. doi: 10.1080/21650373.2022.2149633.
[37] Liu J, et al. 3D-printed concrete with recycled glass: effect of glass gradation on flexural strength and microstructure. Constr Build Mater. 2022;314:125561. doi: 10.1016/j.conbuildmat.2021.125561.
[38] Sambucci M, Valente M. Influence of waste tire rubber particles size on the microstructural, mechanical, and acoustic insulation properties of 3D-printable cement mortars. Civil Eng J. 2021;7(06):937–952. doi: 10.28991/cej-2021-03091701.
[39] Cui W, et al. Study of 3D printed concrete with low-carbon cementitious materials based on its rheological properties and mechanical performances. J Sustain Cem Based Mater. 2023;12(7):832–841. doi: 10.1080/21650373.2023.2189172.
[40] Lu B, et al. Substitution of cement by marine clay in spray-based 3D concrete printing. J Sustain Cem Based Mater. 2024;13(3):375–388. doi: 10.1080/21650373.2023.2278754.
[41] Cui W, et al. Mechanical performance and permeability of low-carbon printable concrete. J Sustain Cem Based Mater. 2025;14(3):406–416. doi: 10.1080/21650373.2024.2374839.
[42] Pasupathy K, Ramakrishnan S, Sanjayan J. 3D concrete printing of eco-friendly geopolymer containing brick waste. Cem Concr Compos. 2023;138:104943. doi: 10.1016/j.cemconcomp.2023.104943.
[43] Over D, et al. An investigation of rheological properties and sustainability of various 3D printing concrete mixtures with alternative binders and rheological modifiers. J Sustain Cem Based Mater. 2025;14(3):521–533. doi: 10.1080/21650373.2024.2409297.
[44] Hou S, et al. Fresh properties of 3D printed mortar with recycled powder. Constr Build Mater. 2021;309:125186. doi: 10.1016/j.conbuildmat.2021.125186.
[45] Ling T-C, Poon C-S, Kou S-C. Influence of recycled glass content and curing conditions on the properties of self-compacting concrete after exposure to elevated temperatures. Cem Concr Compos. 2012;34(2):265–272. doi: 10.1016/j.cemconcomp.2011.08.010.

[46] Zealand ASN, Committee BD-031. Supplementary cementitious materials part 1: fly ash. As/Nzs 3582.1. Australian standard. 2016.
[47] Rivera JF, et al. Novel use of waste glass powder: production of geopolymeric tiles. Adv Powder Technol. 2018;29(12):3448–3454. doi: 10.1016/j.apt.2018.09.023.
[48] Pasupathy K, et al. Carbonation of a blended slag-fly ash geopolymer concrete in field conditions after 8 years. Constr Build Mater. 2016;125:661–669. doi: 10.1016/j.conbuildmat.2016.08.078.
[49] Larson RG, Wei Y. A review of thixotropy and its rheological modeling. J Rheol. 2019;63(3):477–501. doi: 10.1122/1.5055031.
[50] Lootens D, et al. Yield stress during setting of cement pastes from penetration tests. Cem Concr Res. 2009; 39(5):401–408. doi: 10.1016/j.cemconres.2009.01.012.
[51] Vafaei M, Allahverdi A. High strength geopolymer binder based on waste-glass powder. Adv Powder Technol. 2017;28(1):215–222. doi: 10.1016/j.apt.2016.09.034.
[52] Hajimohammadi A, Ngo T, Kashani A. Glass waste versus sand as aggregates: the characteristics of the evolving geopolymer binders. J Clean Prod. 2018;193: 593–603. doi: 10.1016/j.jclepro.2018.05.086.
[53] Pasupathy K, Ramakrishnan S, Sanjayan J. Formulating eco-friendly geopolymer foam concrete by alkali-activation of ground brick waste. J Clean Prod. 2021; 325:129180. doi: 10.1016/j.jclepro.2021.129180.
[54] Wang Y, et al. Effects of Si/Al ratio on the efflorescence and properties of fly ash based geopolymer. J Clean Prod. 2020;244:118852. doi: 10.1016/j.jclepro.2019.118852.
[55] Wang Y, et al. Effect of granulated phosphorus slag on physical, mechanical and microstructural characteristics of class F fly ash based geopolymer. Constr Build Mater. 2021;291:123287. doi: 10.1016/j.conbuildmat.2021.123287.
[56] Tay YWD, Qian Y, Tan MJ. Printability region for 3D concrete printing using slump and slump flow test. Compos Part B. 2019;174:106968. doi: 10.1016/j.compositesb.2019.106968.
[57] Chindaprasirt P, Rattanasak U, Taebuanhuad S. Role of microwave radiation in curing the fly ash geopolymer. Adv Powder Technol. 2013;24(3):703–707. doi: 10.1016/j.apt.2012.12.005.
[58] Tho-In T, et al. Compressive strength and microstructure analysis of geopolymer paste using waste glass powder and fly ash. J Clean Prod. 2018;172:2892–2898. doi: 10.1016/j.jclepro.2017.11.125.
[59] Chen M, et al. Rheological and mechanical properties of admixtures modified 3D printing sulphoaluminate cementitious materials. Constr Build Mater. 2018;189: 601–611. doi: 10.1016/j.conbuildmat.2018.09.037.
[60] Muthukrishnan S, Ramakrishnan S, Sanjayan J. Effect of alkali reactions on the rheology of one-part 3D printable geopolymer concrete. Cem Concr Compos. 2021; 116: 1–22. doi: 10.1016/j.cemconcomp.2020.103899.
[61] Zhong H, Zhang M. 3D printing geopolymers: a review. Cem Concr Compos. 2022;128:104455. doi: 10.1016/j.cemconcomp.2022.104455.
[62] Liu C, et al. Influence of hydroxypropyl methylcellulose and silica fume on stability, rheological properties, and printability of 3D printing foam concrete. Cem Concr Compos. 2021;122:104158. doi: 10.1016/j.cemconcomp.2021.104158.
[63] Sheng Z, et al. Influence of waste glass powder on printability and mechanical properties of 3D printing geopolymer concrete. Dev Built Environ. 2024;20: 100541. doi: 10.1016/j.dibe.2024.100541.
[64] Pasupathy K, Ramakrishnan S, Sanjayan J. Enhancing the properties of foam concrete 3D printing using porous aggregates. Cem Concr Compos. 2022;133:104687. doi: 10.1016/j.cemconcomp.2022.104687.
[65] Le TT, et al. Hardened properties of high-performance printing concrete. Cem Concr Res. 2012;42(3):558–566. doi: 10.1016/j.cemconres.2011.12.003.
[66] Kruger J, Du Plessis A, van Zijl G. An investigation into the porosity of extrusion-based 3D printed concrete. Addit Manuf. 2021;37:101740. doi: 10.1016/j.addma.2020.101740.
[67] Yu S, et al. Microstructural characterization of 3D printed concrete. J Build Eng. 2021;44:102948. doi: 10.1016/j.jobe.2021.102948.
[68] Yu S, Sanjayan J, Du H. Effects of cement mortar characteristics on aggregate-bed 3D concrete printing. Addit Manuf. 2022;58:103024. doi: 10.1016/j.addma.2022.103024.
[69] Liang G, et al. Reuse of waste glass powder in alkali-activated metakaolin/fly ash pastes: physical properties, reaction kinetics and microstructure. Resour Conserv Recycl. 2021;173:105721. doi: 10.1016/j.resconrec.2021.105721.
[70] Rashad AM, Essa GMF, Abdel-Gawwad HA. An investigation of alkali-activated slag pastes containing recycled glass powder under the effect of elevated temperatures. Environ Sci Pollut Res Int. 2022;29(19): 28647–28660. doi: 10.1007/s11356-021-18365-7.
[71] De Silva P, Sagoe-Crenstil K, Sirivivatnanon V. Kinetics of geopolymerization: role of Al2O3 and SiO2. Cem Concr Res. 2007;37(4):512–518. doi: 10.1016/j.cemconres.2007.01.003.